Frictional Ignition of Dissimilar-Metal Sliding Contacts in High-Pressure Oxygen

Andres Garcia Jimenez[1] and Zachary C. Cordero[2]
Massachusetts Institute of Technology, Cambridge, MA, 02139, US

Fabio A. Bendana[3], Timothy M. Wabel[4], and John D. DeSain[5]
The Aerospace Corporation, El Segundo, CA, 90245, US

Sliding contacts between dissimilar metals are found throughout turbomachinery, e.g., in bearings and dynamic seals. In sliding contacts where materials are exposed to high-pressure, high-temperature oxygen – e.g., oxygen-rich turbopumps – frictional heating can result in metal ignition and burning, a potentially catastrophic failure mode. In this paper, we examine the frictional ignition behaviors of dissimilar metal contacts through a combination of frictional ignition experiments, post-test characterization of the rubbing surface on recovered specimens, and complementary finite element analysis of the temperature at the rubbing interface. Dissimilar metal contacts exhibit qualitatively similar sliding behavior to similar-contact metal contacts, i.e., a dramatic reduction in friction coefficient during the early stages of rubbing, resulting from the formation of an oxide tribolayer. In dissimilar metal contacts, a tribolayer can form via oxidation of the parent metal or via material transfer from one specimen to the other. As a result, oxide tribolayers sometimes have disparate chemistry from the parent metal. The formation of this oxide transfer layer depends on the material-pair, sliding conditions, and surface geometry. The steady-state friction coefficient in dissimilar metal contacts is highly sensitive to oxide transfer dynamics and is bounded by the steady-state coefficients of the constituent materials in similar-contact tests. The ignition temperature of the dissimilar metal pair corresponds to the lower ignition temperature of the two alloys. Using a high thermal conductivity metal for the stator delayed ignition by dissipating heat via conduction along the shank of the specimen. The time to ignition is less sensitive to the thermal conductivity of the rotor because convection dominates the rotor cooling behavior. A metric consisting of relevant material properties and considering the effects of contact pressure, sliding speed, and oxygen pressure was developed to determine operating conditions for designing frictional ignition-resistant systems. This parameter has been generalized to various material-pair systems. These insights can be used to guide the design of dissimilar metal contacts that are ignition-resistant and provide a framework for establishing safe operating conditions for specific material combinations.

I. Nomenclature

η = dynamic viscosity, kg/(m·s)
κ = thermal conductivity, W/(m·K)
μ = dynamic friction coefficient
ν = kinematic viscosity, m^2/s
C_p = specific heat capacity, J/(kg·K)

---

[1] Graduate Student, Department of Aeronautics and Astronautics
[2] Associate Professor, Department of Aeronautics and Astronautics
[3] Research Scientist, Propulsion Science Department
[4] Engineering Specialist, Propulsion Department
[5] Sr. Scientist, Propulsion Science Department

D = outer sample diameter, m
F = fin parameter, m^{-1}
h = convective heat transfer coefficient, W/(m^2·K)
l = sample wall thickness, m
P = contact pressure, MPa
q = heat flux, W/m^2
t = time, s
T = temperature, K
T_0 = ambient temperature, K
v = linear sliding speed, m/s
z = axial position along the sample, m
r = subscript indicates rotor
s = Subscript indicates stator

II. Introduction

Next-generation reusable rocket engines will use oxidizer-rich staged combustion (ORSC) and full-flow staged combustion (FFSC) power cycles. These engines improve fuel efficiency compared to traditional gas generator cycle engines. However, they rely on oxygen-rich turbomachinery which subjects materials to high-pressure oxygen environments where this is a risk of metal ignition and burning, a catastrophic failure mode. A potential ignition source is frictional heating at sliding contacts, e.g., in bearings and dynamic seals [1,2]. We recently investigated the frictional ignition behaviors of several engineering alloys through experiments in which identical samples were rubbed against each other in a high-pressure oxygen environment [3]. In these experiments, the friction coefficient decreased with time due to the *in situ* growth of a lubricating oxide tribolayer. Additionally, frictional ignition was directly linked to breakdown of this tribolayer, exposing the hot underlying metal to oxygen. We identified several different tribolayer breakdown mechanisms – melting of the underlying metal, melting of the tribolayer, and mechanical failure of the tribolayer. A key finding from these experiments was that alloy chemistry strongly influences the strength and stability of the tribolayer, which in turn affects frictional ignition resistance.

While this past work provides insights into the ignition behaviors of similar metal contact experiments, the ignition behaviors of dissimilar metal contacts, which are also encountered throughout turbomachinery, are less understood. Based on past observations from low-speed sliding experiments of dissimilar metals, material may transfer from one component to the other during sliding resulting in the formation of transfer tribolayers with disparate chemistry from the base metal [4–8]. These transfer layers can strongly influence the sliding and ignition behaviors. In this paper, we examine the ignition behavior of dry dissimilar metal contacts by performing frictional ignition experiments of dissimilar material pairs under high-pressure oxygen environments. We consider engineering alloys that have a wide range of ignition and combustion behaviors as revealed through past frictional ignition and promoted combustion testing. Experimental results and finite element simulations are used to determine the interfacial temperature during frictional ignition tests. We also characterize the oxide tribolayers that form *in situ*. We extend our analysis to a broad range of dissimilar material-pair combinations and develop a metric to determine operating conditions for designing frictional ignition-resistant systems considering the effects of material properties, contact pressure, sliding speed, and gas pressure. These results can inform the selection of ignition-resistant material pairs for stationary and rotating components in turbomachinery.

III. Frictional ignition experiments

Frictional ignition experiments were performed using a specialized rub rig under an oxygen pressure of 6.9 MPa. In these experiments, two cylindrical samples (one rotating and the other stationary) were rubbed against each other at a constant linear sliding speed of 22 m/s while the contact pressure was increased at 100 kPa/s. Additional details on the experimental setup are provided in [9,10]. Similar-contact tests were performed on three different alloys – Monel K500 (MK500), Ni-20Cr, and Inconel 718 (IN718). Their compositions are summarized in **Table 1**. These alloys are of interest because they exhibit a range of ignition behaviors: Ni-20Cr is intrinsically ignition resistant while IN718 has poor ignition resistance. We assessed two different dissimilar material pairs – IN718 vs. Ni-20Cr and MK500 vs. Ni-20Cr.

Table 1: Nominal composition of alloys tested.

Alloy	Composition (wt%)								
	Ni	Fe	Cr	Cu	Al	Mo	Mn	Nb	Ti
Monel K500	63	2		30	3		2		0.5
Ni-20Cr	80		20						
Inconel 718	53	19	19		0.4	3		5	0.9

The rubbing surfaces of recovered samples were inspected visually and imaged using optical and electron microscopy. Non-ignited samples were cross-sectioned, mechanically polished, and imaged using scanning electron microscopy (SEM). X-ray diffraction using a cobalt x-ray source and energy-dispersive x-ray spectroscopy (EDS) were used to determine the phases at the rubbing interface.

IV. Frictional heating simulations

We used finite element simulations to compute the temperature field within the test specimens during the frictional ignition experiments [3,11]. Experimental measurements of friction coefficient and contact load were used with the known material properties and specimen geometry to compute the interfacial temperature during rubbing. **Fig. 1** depicts the simulation domain and boundary conditions. The simulation domain explicitly included the rotor, including convective heat transfer on its side surfaces to account for the effects of high-speed rotation. The convective heat transfer coefficient, h, was estimated using the correlation developed by Anderson and Saunders [12] for a cylinder rotating along its longitudinal axis in quiescent air,

$$h = 0.28\left(\frac{v^2}{D}\frac{C_p \eta \kappa_{O_2}^2}{\nu^2}\right)^{1/3}, \tag{1}$$

where v is the surface speed of the rotor (22 m/s), κ_{O_2} is the thermal conductivity of gaseous O_2, ν is the kinematic viscosity of O_2, η is the dynamic viscosity of O_2, C_p is the specific heat capacity of O_2, and D is the outer diameter of the sample. Note that the properties of O_2 gas are temperature- and pressure-dependent and were obtained from the literature for the pressure of interest (6.9 MPa) [13–16]. There was no interfacial thermal resistance at the gas/solid interface of the stator. The FEM also considered heat conduction in the solids and gaseous oxygen as well as radiative heat transfer between the samples and the chamber walls. Energy balance and temperature continuity at the rubbing interface were enforced, with an interfacial frictional heat flux boundary condition given by

$$q = \mu P v, \tag{2}$$

where μ is the dynamic friction coefficient, P is the contact load, and v is the average linear sliding speed of 22 m/s. The material properties, including the density ρ, thermal conductivity κ, specific heat capacity C_p, and emissivity e are summarized in **Table 2**.

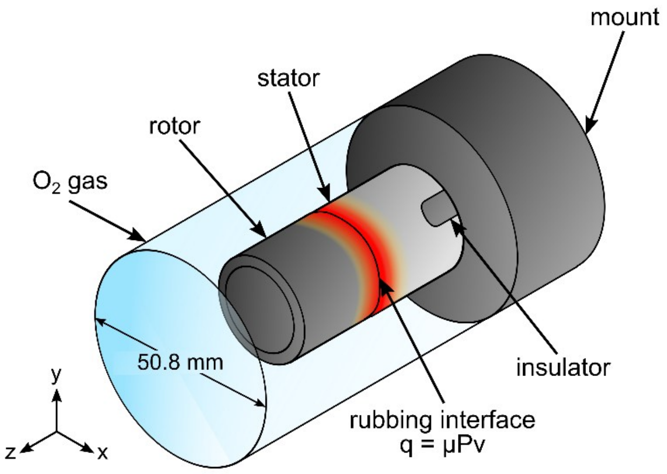

Fig. 1: Frictional heating FEM in COMSOL Multiphysics [17].

Table 2: Material properties of the different materials at room temperature.

Alloy	ρ (kg/m^3)	κ (W/(m·K))	C_p (J/(kg·K))	e
Monel K500	8160	17.5	520	0.4
Ni-20Cr	8400	15.0	448	0.5
Inconel 718	8190	11.4	435	0.3

V. Experimental results and discussion

In this section, we discuss the experimental results for each of the dissimilar material tests and compare them to general trends observed in similar-contact material experiments. Additionally, we characterize the oxide tribolayers on non-ignited samples to analyze the effects of sliding conditions and parent material chemistry on the oxide structures formed during sliding of dissimilar materials tests. These observations relate oxide structure to the onset of ignition, highlighting the ignition mechanisms for each sliding system. We indicate the test configuration with the convention stator/rotor. As an example, IN718/Ni-20Cr refers to a dissimilar test where IN718 was the rotor and Ni-20Cr the rotor.

A. Dissimilar sliding contacts between IN718 and Ni-20Cr

Table 3 summarizes the experimental results from the dissimilar and similar-contact experiments between IN718 and Ni-20Cr. The IN718 similar-contact test ignited at 38 s while the similar-contact test of Ni-20Cr took longer to ignite (115 s). Both dissimilar contact experiments between IN718 and Ni-20Cr resulted in ignition, with the Ni-20Cr/IN718 test igniting at 52 seconds, and the IN718/Ni-20Cr test igniting at 38 sec, the same ignition time as the similar-contact IN718 test. This result suggests that judicious selection of the stator and rotor materials can delay ignition.

Table 3: Results from dissimilar frictional ignition tests between IN718 and Ni-20Cr

Stator Material	Rotor Material	t_{ign} (s)	μ_{ss}	T_{ign} (K)
Inconel 718	Inconel 718	38	0.044	1000
Inconel 718	Ni-20Cr	38	0.046	930
Ni-20Cr	Inconel 718	52	0.041	1080
Ni-20Cr	Ni-20Cr	115	0.030	1630

Fig. 2 shows the friction coefficient vs. time measured in both dissimilar- and similar-contact experiments. In all tests, the friction coefficient curves begin with initial values in the range of 0.10–0.25 and decay exponentially to lower steady-state values between 0.04–0.045 (cf. **Table 3**). After this initial decay, all tests ignite except for the Ni-20Cr similar-contact test, where the friction coefficient continues to decrease to a steady-state value of 0.03 (cf. **Table 3**). In our previous work on frictional ignition of Ni-Cr alloys [3], we directly linked this decay in the friction coefficient to the *in situ* growth of an oxide tribolayer at the rubbing interface. In each test, there is an abrupt increase in the friction coefficient prior to ignition as the tribolayer breaks down and the underlying metals form junctions.

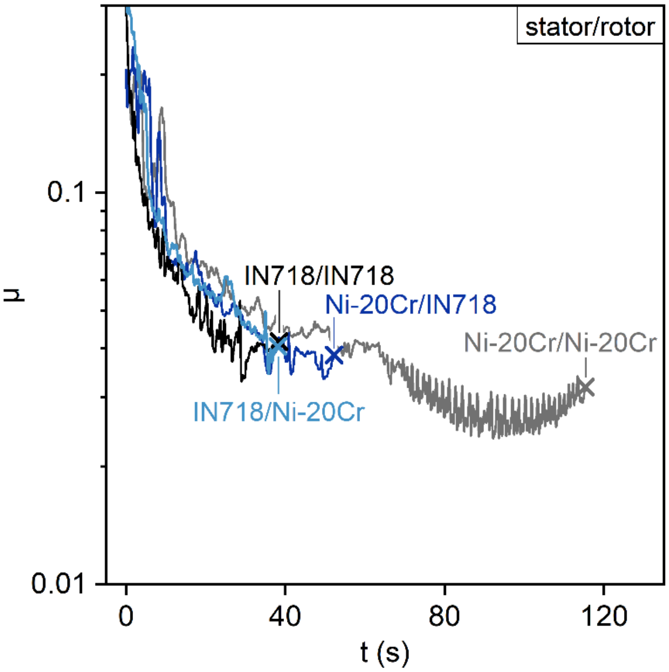

Fig. 2: Friction coefficient vs. time for IN718 and Ni-20Cr in dissimilar and similar-contact tests. Cross marks indicate the test resulted in ignition.

The calculated interfacial temperatures for Ni-20Cr and IN718 during both dissimilar and similar-contact experiments are plotted as a function of time in **Fig. 3**. Initially, the interfacial temperature rises rapidly due to the high friction coefficient. As the friction coefficient decays the steady-state value, the heating rate decreases. The temperatures at ignition (see **Table 3**) vary, ranging from a low of 930 K in the IN718/Ni-20Cr dissimilar test to a high of 1630 K in the Ni-20Cr similar-contact experiment. Ignition temperatures of the dissimilar tests were: 1080 K for Ni-20Cr/IN718 and 930 K for IN718/Ni-20Cr; both ignition temperatures closely match that of IN718 in the similar-contact test, which was 1000 K. Interestingly, these ignition temperatures are significantly lower than the melting points of both materials, 1674 K for Ni-20Cr and 1533 K for IN718. In previous work [3], we suggested that the dominant frictional ignition mechanism for materials igniting well below their melting points is mechanical breakdown of the protective tribolayer. This same mechanism likely governs the ignition observed in the dissimilar tests involving Ni-20Cr and IN718, where the mechanical breakdown of the tribolayer on the IN718 sample exposes the hot underlying metal to high-pressure oxygen, triggering ignition. By contrast, under an O_2 pressure of 6.9 MPa, Ni-20Cr ignites at temperatures close to its melting point, indicating that its dominant ignition mechanism is melting of the underlying metal, resulting in tribolayer breakdown. Note that post-mortem observations of the ignited samples in all dissimilar tests involving IN718 and Ni-20Cr showed that once ignited, both samples sustained combustion with the stationary sample exhibiting a higher degree of damage. This suggests that even if the material with lower ignition resistance (IN718) ignites first, the reaction may quickly kindle to the more ignition-resistant material (Ni-20Cr) potentially resulting in failure of the entire sliding system.

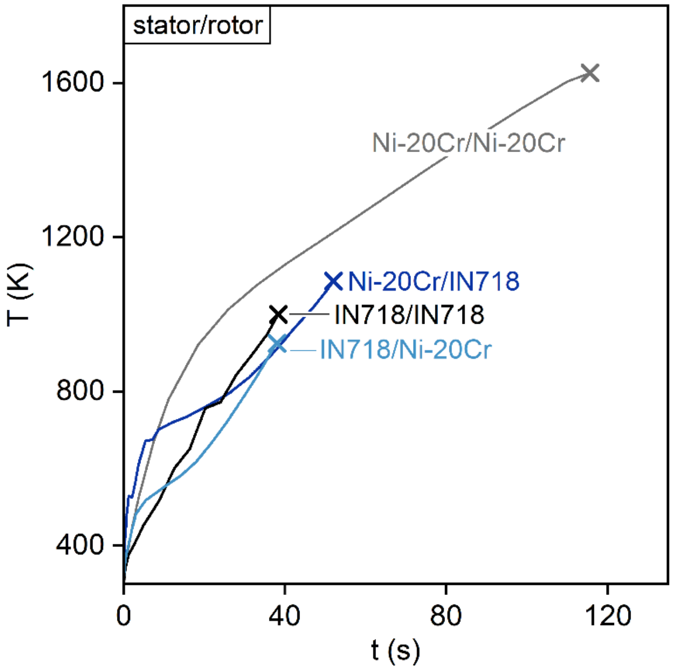

Fig. 3: Interfacial temperature vs. time for IN718 and Ni-20Cr in dissimilar- and similar-contact tests. Crosses indicate ignition.

Comparing the ignition behaviors across different tests highlights the effects of material chemistry, thermodynamic properties, and dissimilar contacts on ignition resistance. In the Ni-20Cr/IN718 test, the ignition time was longer than the IN718 similar-contact test but shorter than the Ni-20Cr similar-contact test. This difference is due to the higher thermal conductivity of Ni-20Cr (15 $Wm^{-1}K^{-1}$ vs. 11 $Wm^{-1}K^{-1}$ for IN718), which results in a faster rate of heat dissipation from the rubbing surface via conduction, delaying the time required to reach the ignition temperature. However, this delay in ignition time was not observed when Ni-20Cr served as the rotor material in the IN718/Ni-20Cr test, which ignited at the same time as the IN718 similar-contact test. **Fig. 4** compares the temperature profiles along the axial length of the samples for the dissimilar tests at t = 35 s. The temperature along the length of the stator in the Ni-20Cr/IN718 test is higher than in the IN178/Ni-20Cr test, indicating that the dominant cooling mechanism of the stator is conduction. Thus, using the high thermal conductivity specimen as the stator helps dissipate heat and delay ignition.

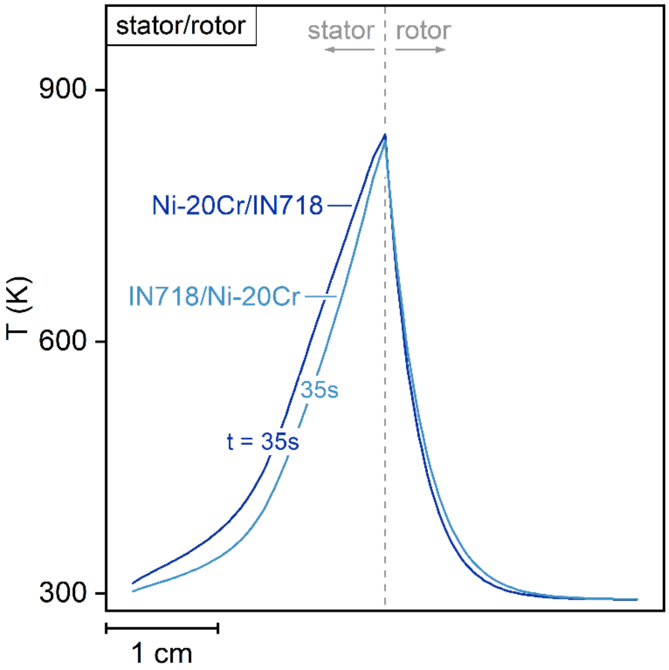

Fig. 4: Temperature profile along the axial length of the samples in the dissimilar experiments between IN718 and Ni-20Cr at t = 35 s.

Fig. 5 shows the axial specimen deformation in the different tests. This measurement reflects the combined effects of plastic deformation, wear, and thermal expansion. Ni-20Cr in the similar-contact test exhibited the highest degree of deformation because: (i) it has a relatively low strength; (ii) it was subjected to the highest contact pressure; and (iii) it reached the highest interfacial temperature. Notably, the deformation behaviors of the Ni-20Cr/IN718 and Ni-20Cr similar-contact tests follow the same trend characterized by monotonic compression during sliding. Similarly, the IN718/Ni-20Cr and IN718 similar-contact tests have the same deformation behavior consisting of an initial period of compressive deformation, followed by thermal expansion as the rubbing surface reaches elevated temperatures. Such behavior is typical of the "rubbing-in" phase during the early stages of sliding between components.

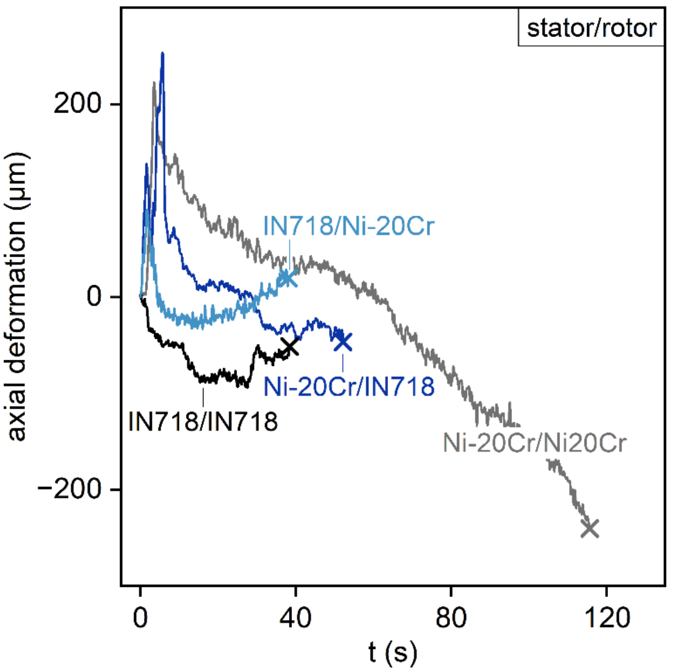

Fig. 5: Axial deformation vs. time for IN718 and Ni-20Cr in dissimilar and similar-contact tests. Cross marks indicate the test resulted in ignition.

B. Dissimilar sliding contacts between MK500 and Ni-20Cr

Experimental results from the dissimilar and similar-contact experiments between Monel K500 and Ni-20Cr are summarized in **Table 4**. The ignition times in similar-contact experiments ranged from 52 s for MK500 to 115 s for Ni-20Cr. Of the dissimilar tests only the Ni-20Cr/MK500 resulted in ignition, which ignited at 55 s, closely matching the ignition time of the MK500 similar-contact test. By contrast, the MK500/Ni-20Cr test did not ignite. The results from the dissimilar tests between MK500 and Ni-20Cr suggest that when Ni-20Cr served as the stator there was no effect on ignition resistance compared to the MK500 similar-contact tests. By contrast, when Ni-20Cr was the rotor, ignition was mitigated altogether. The above trends in the dissimilar tests between MK500 and Ni-20Cr are contrary to those observed in the dissimilar tests between IN718 and Ni-20Cr, where instead we observed that using Ni-20Cr as the rotor material had no effect on ignition resistance while using Ni-20Cr as the stator material improved ignition resistance compared to the IN718 similar-contact test.

Table 4: Results from dissimilar frictional ignition tests between Monel K500 and Ni-20Cr

Stator Material	Rotor Material	t_{ign} (s)	μ_{ss}	T_{ign} (K)
Monel K500	Monel K500	52	0.047	1580
Monel K500	Ni-20Cr	120*	0.034*	1330*
Ni-20Cr	Monel K500	54	0.048	1530
Ni-20Cr	Ni-20Cr	115	0.030	1630

*No ignition

Fig. 6 shows the friction coefficient vs. time measured in dissimilar- and similar-contact tests between MK500 and Ni-20Cr. As in the dissimilar tests involving IN718 and Ni-20Cr (cf. **Fig. 2**), all friction coefficient curves decay exponentially to lower steady-state values between 0.045–0.05 (see **Table 4**) due to the growth of an oxide tribolayer. After this initial decay, the Ni-20Cr/MK500 and MK500 similar-contact tests ignite while the friction coefficient of the MK500/Ni-20Cr and Ni-20Cr similar-contact tests continue to decrease to lower steady-state values of 0.03–0.034 (see **Table 4**). Note that in the MK500/Ni-20Cr test, there is a rise in the friction coefficient at around 80-90 seconds potentially reflecting tribolayer breakdown during sliding. Interestingly, when comparing the steady-state friction coefficients of dissimilar tests between IN718 and Ni-20Cr from **Table 3** and of dissimilar tests involving MK500 and Ni-20Cr from **Table 4**, we observe that in both sliding systems the friction coefficients are bounded by the individual friction coefficients of the rotor and stator materials in similar-contact tests.

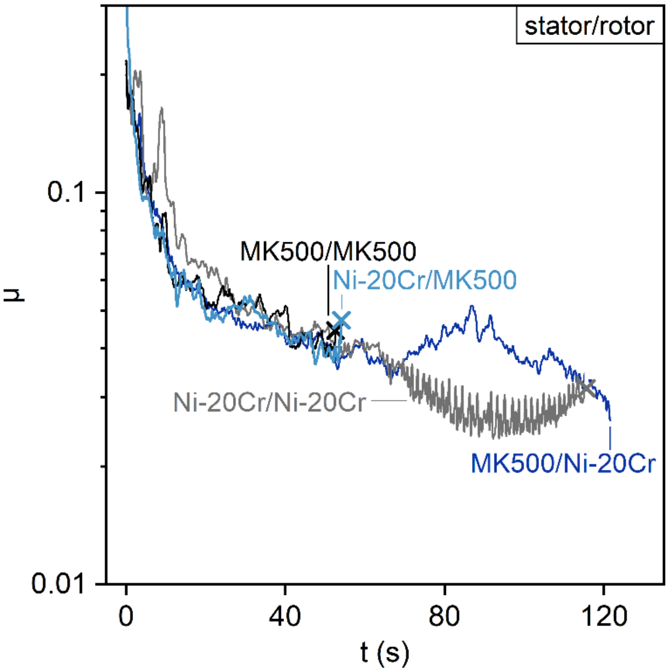

Fig. 6: Friction coefficient vs. time for MK500 and Ni-20Cr in dissimilar and similar-contact tests. Cross marks indicate the test resulted in ignition.

Fig. 7 shows the calculated interfacial temperature vs. time for MK500 and Ni-20Cr during dissimilar and similar-contact experiments. **Table 4** includes the surface temperatures at ignition. The Ni-20Cr/MK500 test ignited at 1530 K, closely aligning with the ignition temperature of the MK500 similar-contact test (1580 K) – both near the melting point of MK500 (1590 K). Based on these results and our previous work [3], MK500 in the Ni-20Cr/MK500 test and similar-contact test ignites due to melting of the underlying metal, resulting in tribolayer breakdown. As in the dissimilar tests between IN718 and Ni-20Cr (cf. **Section A**), characterization of ignited samples in the Ni-20Cr/MK500 test indicated that both rotor and stator sustained combustion, suggesting that once MK500 ignited, the reaction kindled to the Ni-20Cr sample. By contrast, the MK500/Ni-20Cr test did not ignite because the peak interfacial temperature of 1330 K is well below the ignition temperatures of both MK500 and Ni-20Cr. This low peak interfacial temperature is primarily due to the lower friction coefficient in the dissimilar experiment (0.034 vs. 0.048 in Ni-20Cr/MK500). Below we show that this low friction coefficient is due to material transfer from one sample to the other one during sliding. Altogether, the above results from the dissimilar tests between IN718 and Ni-20Cr and between MK500 and Ni-20Cr suggest that the ignition temperature of a sliding system with dissimilar materials is determined by the material with the lower ignition temperature from similar-contact tests.

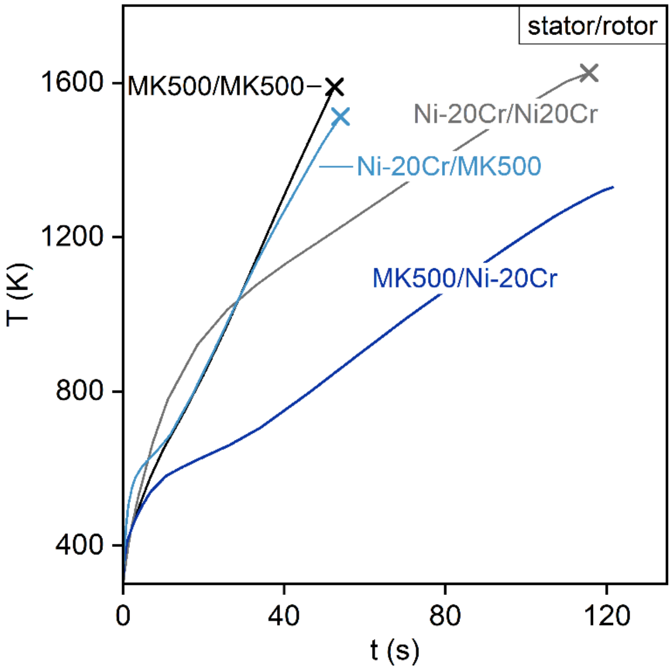

Fig. 7: Interfacial temperature vs. time for MK500 and Ni-20Cr in similar-contact and dissimilar materials tests. Cross marks indicate the test resulted in ignition.

The temperature profiles along the axial length of the samples for the dissimilar tests between MK500 and Ni-20Cr are shown in **Fig. 8** at select test times (*t*). At *t* = 40 s, the interfacial temperature in the Ni-20Cr/MK500 test was ~1050 K, which is ~300 K higher than that of the MK500/Ni-20Cr test. This temperature difference is due to the lower friction coefficient in the MK500/Ni-20Cr test. Notably, at this same test time, the magnitude of the temperature gradient along the stator sample in the Ni-20Cr/MK500 test is larger than in the MK500/Ni-20Cr test, suggesting a higher degree of conduction in the MK500/Ni-20Cr test. This aligns with the fact that MK500 has higher thermal conductivity than Ni-20Cr (see **Table 2**).

By comparing the temperature profiles in the dissimilar materials tests between MK500 and Ni-20Cr when the interfacial temperatures are the same (i.e., the Ni-20Cr/MK500 curve at *t* = 40 s vs. the MK500/Ni-20Cr broken curve at *t* = 80 s, see **Fig. 8**) we observe that the temperature profiles in the rotor samples are similar. This behavior was also observed in the dissimilar tests between IN718 and Ni-20Cr (**Fig. 4)**, which further corroborates that the dominant cooling mechanism of the rotor is convection to the gas. Additionally, the stator temperature profile in the MK500/Ni-20Cr test (*t* = 80 s) is higher than in the Ni-20Cr/MK500 test agreeing with our previous observation that the dominant cooling mechanism of the stator is solid-state conduction.

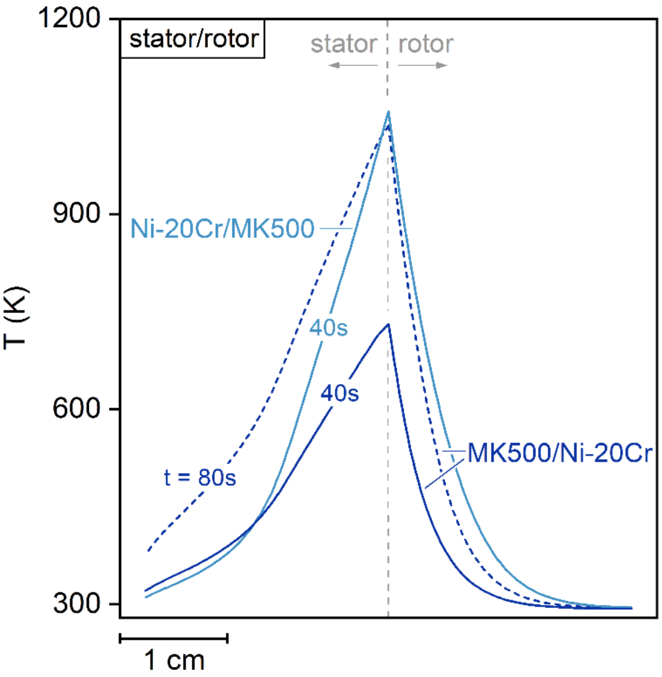

Fig. 8: Temperature profile along the axial length of the samples in the dissimilar experiments between MK500 and Ni-20Cr at select test times (t).

Fig. 9 shows the axial deformation measured in dissimilar and similar-contact tests between MK500 and Ni-20Cr. The MK500 similar-contact test exhibited the least deformation, while the MK500/Ni-20Cr test showed the highest degree of deformation. The deformation behaviors in the Ni-20Cr/MK500 test and in the MK500 similar-contact test were similar, consisting of initial compressive deformation, followed by expansion, and concluding with further compression. In contrast, we observe monotonic compressive deformation in the MK500/Ni-20Cr test. The discrete compressive displacement observed around 80–90 s in the MK500/Ni-20Cr test likely represents tribolayer breakdown, aligning with the rise in friction coefficient at the same test time, as shown in **Fig. 6**. MK500/Ni-20Cr test did not ignite during this initial period of tribolayer breakdown because the interfacial temperature remained well below the ignition temperatures of MK500 and Ni-20Cr. Finally, we observe no clear trends in the deformation behaviors across the different tests (dissimilar tests between IN718 and Ni-20Cr and dissimilar tests involving MK500 and Ni-20Cr) suggesting that the deformation behavior of the sliding system depends on the given stator/rotor material-pair.

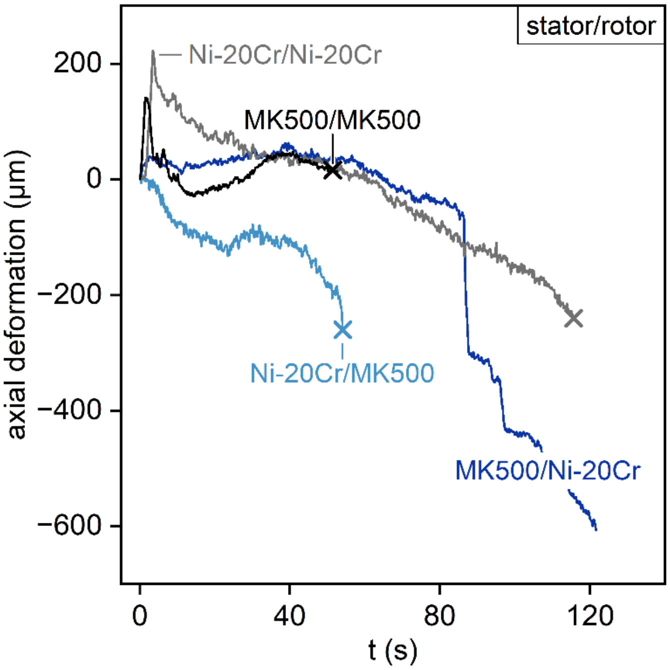

Fig. 9: Axial deformation vs. time for MK500 and Ni-20Cr in similar-contact and dissimilar materials tests. Cross marks indicate the test resulted in ignition.

In light of the above results, we characterized the rubbing surfaces on the non-ignited samples of the MK500/Ni-20Cr test to understand why this specific material-pair combination did not ignite. **Fig. 10a** shows an SEM micrograph of the oxide tribolayers formed on MK500 (stator) and Ni-20Cr (rotor). Both tribolayers exhibit a stratified structure, with the tribolayer on MK500 having an average thickness of 210 µm, which is ~85 µm thicker than the tribolayer on Ni-20Cr. Both oxide tribolayers display through-thickness cracks. The through-thickness cracks on the Ni-20Cr tribolayer are likely caused by high thermal stresses and incompatible deformation between the brittle oxide tribolayer and the more ductile underlying metal. The through-thickness cracks on the MK500 tribolayer likely result from the compressive contact stresses acting upon the brittle oxide adhered to a plastically deforming substrate. Additionally, we observe cracks parallel to the oxide/metal interface, particularly between the interlayers of different oxide phases. These parallel cracks are attributed to compressive stresses induced during cooling upon test shutdown. There is no microstructural evidence of melting in either the oxide layers or the underlying metals.

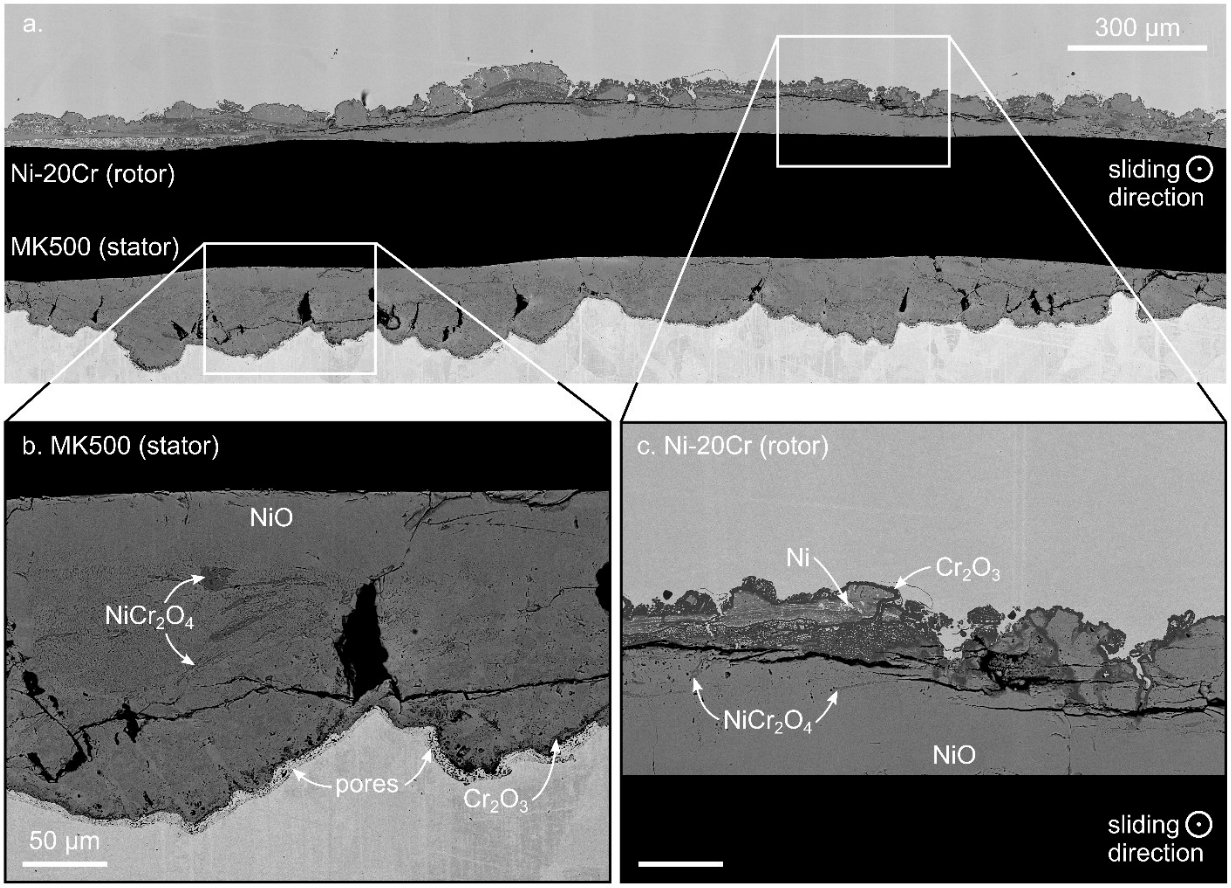

Fig. 10: (a) Oxide tribolayers formed on the non-ignited samples of the Ni-20Cr rotor vs. MK500 stator frictional ignition test. High magnification micrograph of highlighted section of the tribolayer on (b) MK500 stator and (c) Ni-20Cr rotor.

X-ray diffraction scans for both the rotor and stator shown in **Fig. 11** reveal that the main phases in both tribolayers are NiO and $NiCr_2O_4$. EDS mapping of the tribolayers shown in **Figs. 10b** and **10c** corroborates the XRD results, showing that both tribolayers exhibit a similar phase distribution, which consists of a compact outer layer of equiaxed NiO grains with an average size of 6 µm, followed by a layer of NiO containing nanoscale precipitates of $NiCr_2O_4$. MK500 does not contain any Cr, but its tribolayer contains $NiCr_2O_4$ precipitates, an oxide phase expected to grow only on Ni-Cr alloys, indicating that there was significant material transfer from Ni-20Cr to MK500 during sliding. Another feature that points towards the formation of the tribolayer on MK500 through material transfer is the oxide/metal interface. The MK500 tribolayer shows a highly porous oxide/metal interface decorated with small Cr_2O_3 and $NiCr_2O_4$ precipitates. Similar porous interfaces have been observed on transfer layers formed during low-speed sliding of dissimilar metals in atmospheric air [5,18]. By contrast, the tribolayer on Ni-20Cr features a thin, continuous 1-3 µm interlayer of Cr_2O_3, which forms via diffusional processes [19,20].

The tribolayer structure observed on Ni-20Cr is consistent with that observed in similar-contact frictional ignition experiments of Ni-20Cr under an O_2 pressure of 6.9 MPa [3]. In our previous work, we established that the specific structure and properties of the Ni-20Cr tribolayer give rise to its low friction coefficient and prevent tribolayer breakdown and ignition [3]. The tribolayer on MK500 differs from those observed in similar-contact experiments, where the typical oxide structure consists of an outer Cu_2O and NiO followed by an interlayer of NiO and Ni-Cu solid solution at the oxide/metal interface [21]. Instead, the tribolayer on MK500 in the MK500/Ni-20Cr test has no Cu-bearing oxides and has a structure similar to the tribolayer on Ni-20Cr. This is consistent with the low friction coefficient measured during the

MK500/Ni-20Cr test, which closely matches that of Ni-20Cr in similar-contact tests. This extensive oxide transfer from Ni-20Cr to MK500 allows the formation of a thick and mechanically stable tribolayer on MK500 that effectively lubricates the rubbing interface and mitigates ignition.

The above results indicate that the steady-state friction coefficient in the dissimilar tests depends on material transfer during sliding. Material transfer has also been observed to occur in low-speed sliding experiments of dissimilar metals [4–8]. In these experiments, the friction coefficient also depends on the extent of material transfer during sliding. However, no concrete trend has been established on how material transfers from one component to the other. Instead, it has been observed that material transfer depends on the specific rotor/stator material-pair, surface geometry, and sliding conditions (e.g., contact pressure, sliding speed) [4,7,22]. Further testing and characterization of tribolayers on interrupted samples are required to understand how material transfer occurs for an individual material-pair during frictional ignition.

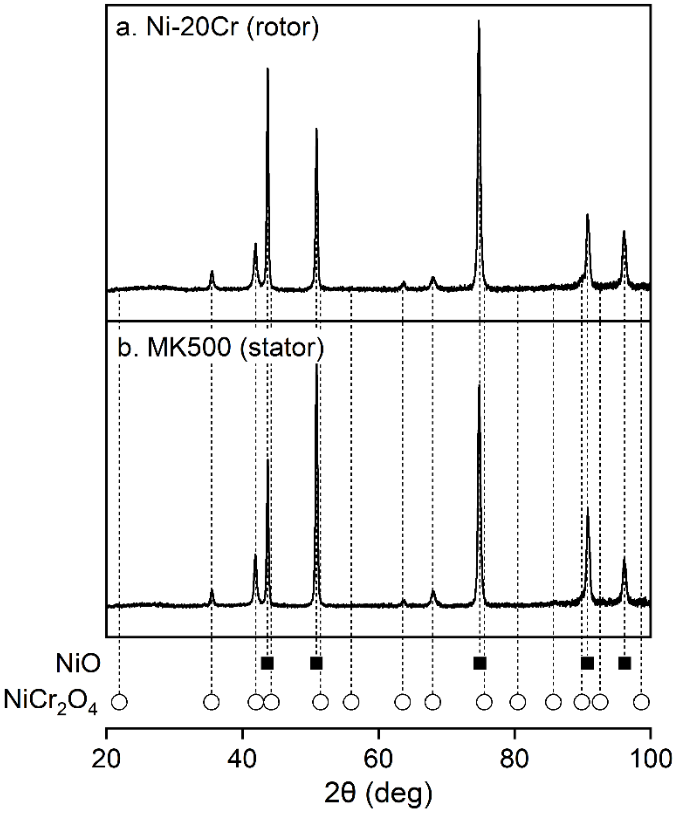

Fig. 11: X-ray diffraction scans of the oxide tribolayers on (a) Ni-20Cr rotor and (b) MK500 stator collected from the non-ignited samples of the MK500/Ni-20Cr test using a Co x-ray source.

VI. Bounds on safe operating conditions for dissimilar material contacts

There are three key findings from the dissimilar tests between IN718 and Ni-20Cr and between MK500 and Ni-20Cr discussed in **Section V**. First, the ignition temperature of the dissimilar-material sliding system is governed by the material with the lowest ignition temperature from similar-contact tests. Second, the friction coefficient of the sliding system is bounded by the friction coefficients of the constituent materials from similar-contact experiments. The friction coefficient of the sliding system reflects material transfer between components, and this transfer process depends on the stator/rotor material-pair, surface geometry, and sliding conditions. Finally, under the given test conditions, the dominant cooling mechanism in the rotor is convection to the gas while in the stator is conduction through the material. Note that the cooling mechanism may vary under different operating conditions.

Based on the key results summarized above, we aim to establish the operating bounds under which a sliding system can function without igniting. To achieve this, we first start by determining the steady-state interfacial temperature, which is the maximum interfacial temperature under a constant heat flux boundary condition, to assess whether the system will ignite, i.e., when the interfacial temperature surpasses the ignition temperature. Given that the wall thickness (l) of both the rotor and stator is 2.54 mm and using **Eq. 1** to calculate the heat transfer coefficient, we estimate the Biot number ($\mathrm{Bi} = hl/\kappa$) for both samples to be in the order of 0.01, indicating that the samples can be approximated as fins. Thus, we approximate the specimens using the one-dimensional, constant cross-section fin approximation, assuming each specimen represents a semi-infinite domain.

The governing equation is

$$\frac{d^2T}{dz^2} = F^2(T - T_0), \tag{3}$$

where z is the axial position along the length of the sample and T_0 is ambient temperature. In **Eq. 3**, F is the fin parameter,

$$F = \left(\frac{h}{\kappa l}\right)^{1/2}, \tag{4}$$

where l is the sample thickness, h is the convective heat transfer coefficient and κ is the thermal conductivity. The stator and rotor have unique fin parameters (F_s and F_r, respectively) because they have different thermal conductivities and heat transfer coefficients. For the rotor, we assume the heat transfer coefficient described by Anderson and Saunders [12] given in **Eq. 1**. For the stator we assume a heat transfer coefficient of 100 $\mathrm{Wm^{-2}K^{-1}}$, which corresponds to free convection on a stationary cylinder with a diameter of 2.54 cm [12]. We also assume that the temperature far away from the rubbing surface ($z_{surf} = 0$) approaches ambient temperature T_0,

$$T_{r,s}(z \to \pm\infty) = T_0. \tag{5}$$

Eq. 5 is valid when the thermal diffusion depth is shorter than the length of the sample. Using scaling analysis, we estimate that the maximum thermal diffusion depth in the rotor materials over the whole test duration is ~1–2 cm, shorter than the sample length (2.54 cm). While the maximum thermal diffusion depth in the stator (2–5 cm) is larger than the sample length, we still use the assumption in **Eq. 5** because the stator is attached to the pressure vessel, which acts as a heat sink due to its large thermal mass. In practical applications, different boundary conditions may be considered to more accurately describe the temperature profile in the sliding components. Finally, at the interface, we enforce temperature continuity,

$$T_r(z_{surf}) = T_s(z_{surf}), \tag{6}$$

as well as energy conservation accounting for the frictional heat flux from **Eq. 2**,

$$\kappa_r \frac{dT_r}{dz}\bigg|_{z_{surf}} - \kappa_s \frac{dT_s}{dz}\bigg|_{z_{surf}} = \mu P v. \tag{7}$$

Using **Eqs. 3–7**, we evaluate the steady-state temperature in both the rotor and stator,

$$T_{r,s} = \frac{\mu P v}{\kappa_r F_r + \kappa_s F_s} e^{\mp F_{r,s} z} + T_0 = \mu P v \left(\frac{l^{1/2}}{(\kappa_r h_r)^{1/2} + (\kappa_s h_s)^{1/2}}\right) e^{\mp F_{r,s} z} + T_0. \tag{8}$$

From **Eq. 8** we observe that the steady-state temperature in both the stator and rotor is the highest at the interface and decays exponentially as we move away from the interface. The extent of the temperature decay depends on the fin parameter with a larger fin parameter indicating a more pronounced decay. The form of the temperature profiles in **Eq. 8** agrees with the temperature profiles calculated using the FEA shown in **Figs. 4** and **8**. By evaluating **Eq. 8** at $z_{surf} = 0$, we obtain the maximum temperature at the rubbing interface under a constant frictional heat flux boundary condition,

$$T_{surf} = \frac{\mu P v}{\kappa_r F_r + \kappa_s F_s} + T_0 = \mu P v \left(\frac{l^{1/2}}{(\kappa_r h_r)^{1/2} + (\kappa_s h_s)^{1/2}} \right) + T_0. \tag{9}$$

To assess whether the sliding system will ignite, we consider that ignition occurs when the maximum interfacial temperature is greater than the ignition temperature of the sliding system,

$$T_{surf} \geq T_{ign}. \tag{10}$$

By combining **Eqs. 9** and **10**, we can determine a relationship between the maximum allowable contact pressure (P_{ign}) and sliding speed,

$$P_{ign} = \frac{T_{ign} - T_0}{\mu v} (k_r F_r + k_s F_s) = \left(\frac{T_{ign} - T_0}{\mu v} \right) \left(\frac{(\kappa_r h_r)^{1/2} + (\kappa_s h_s)^{1/2}}{l^{1/2}} \right). \tag{11}$$

This maximum allowable contact pressure in **Eq. 11** defines the threshold at which the system transitions from safe operation to ignition. When the contact pressure exceeds this threshold, ignition sets on. For sliding between dissimilar materials, the ignition temperature in **Eq. 11** corresponds to the lower ignition temperature of the constituent materials from similar-contact tests. Additionally, the friction coefficient is bounded by the friction coefficients of the constituent materials from similar-contact experiments. The friction coefficient depends on the transfer layer that forms during sliding and the process of how this transfer layer forms depends on the stator/rotor material-pair, surface geometry as well as on operating conditions. Note that the expression in **Eq. 11** assumes the contact geometries between the samples are the same. **Eq. 11** must be modified for applications with different contact geometries.

To validate the expression in **Eq. 11**, we used the measured steady-state friction coefficient, and the calculated ignition temperatures to determine P_{ign} for the dissimilar sliding systems in this study. For the MK500/Ni-20Cr test that did not ignite, the ignition temperature of MK500 from similar-contact tests was used in evaluating P_{ign}. **Fig. 12** shows the maximum allowable contact pressure as a function of sliding speed for the dissimilar material tests. The measured contact pressure at ignition for the dissimilar experiments is also plotted in **Fig. 12**, where crosses indicate the tests that ignited. These experiments were performed under a sliding speed of 22 m/s. For all cases where ignition occurred, the measured contact pressure exceeded the predicted value, indicating that the P_{ign} metric can be used to estimate safe operating conditions. In the MK500/Ni-20Cr test that did not ignite, the maximum contact pressure remained below the predicted maximum allowable contact pressure, confirming the accuracy of the P_{ign} metric in identifying safe operating limits.

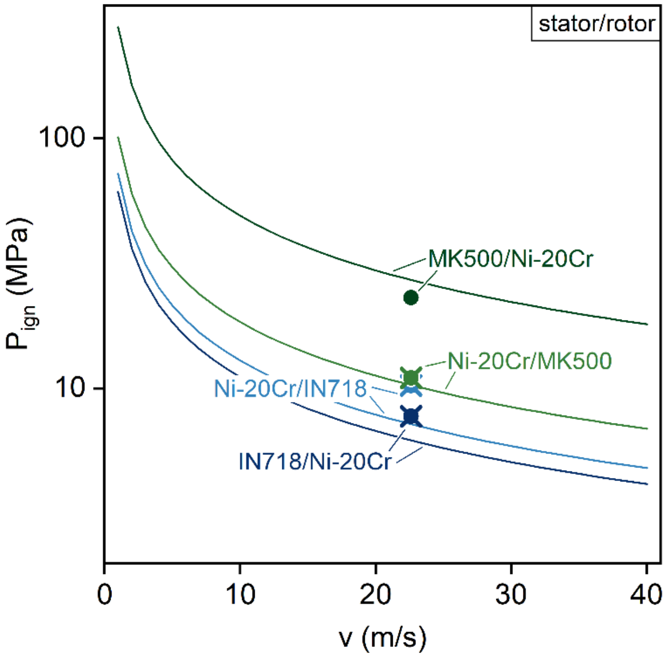

Fig. 12: Maximum allowable contact pressure vs. sliding speed for dissimilar experiments. Operating conditions below the curve will not result in ignition. Crosses indicate tests that ignited.

From **Eq. 11**, the influence of material properties on the maximum allowable contact pressure and ignition resistance becomes evident. A higher ignition temperature, lower friction coefficient, and higher thermal conductivity collectively maximize P_{ign}, thereby expanding the range of safe operating conditions. Materials with these advantageous properties exhibit high maximum allowable contact pressures. This aligns with the experimental results in **Section V** where we observed that Ni-20Cr in similar-contact tests ignites at a contact pressure of 21.9 MPa due to its high ignition temperature and low friction coefficient. By contrast, IN718 exhibits the lowest contact pressure at ignition (7.8 MPa) because it has a high friction coefficient, low thermal conductivity, and low ignition temperature.

The above metric suggests strategies to widen the range of safe operating conditions and enhance the ignition resistance of the sliding system. Selecting materials that have high thermal conductivity or modifying alloy chemistry to improve thermal conductivity can raise P_{ign} and broaden safe operating limits. A more significant increase in P_{ign} can be achieved by enhancing the heat transfer coefficient. As shown in **Eq. 11**, the thermal conductivity (on the order of 10 $Wm^{-1}K^{-1}$ for Ni-base superalloys) is weighted by the heat transfer coefficient, which ranges from 10^2-10^4 $Wm^{-2}K^{-1}$ for O_2 gas under typical service pressures (6.9-69 MPa) [12,23] and can be as high as 10^5 $Wm^{-2}K^{-1}$ for liquid oxygen [24]. Thus, selecting a cooling fluid with a higher convective heat transfer coefficient can further extend the range of safe operating conditions. This strategy is commonly used in bearings, which are flooded with liquid oxygen to reduce overheating and prevent frictional ignition. Modifying surface geometry can also improve the maximum allowable contact pressure. For example, increasing the contact area to reduce localized heating or optimizing sample geometry to incorporate other cooling mechanisms (e.g., impingement jet cooling or film cooling) can significantly improve heat dissipation and raise the maximum allowable contact pressure. Finally, selecting material-pair combinations that form thick, protective, and lubricating transfer layers can help mitigate ignition as seen in the MK500/Ni-20Cr test. However, additional individual testing of material combinations is essential because material transfer dynamics depend on the specific stator/rotor material-pair, operating conditions, and surface geometry.

VII. Generalized material selection principles for ignition-resistant sliding systems

We extend our analysis to additional material-pair systems by generalizing the application of the maximum allowable contact pressure metric from **Eq. 11**, allowing us to identify trends in the ignition behavior of dissimilar materials. To evaluate **Eq. 11**, we must determine both the ignition temperature and friction coefficient for each material pair. From **Section V**, the ignition temperature of a sliding system is governed by the material with the lowest ignition temperature in similar-contact tests. Additionally, the friction coefficient in dissimilar materials contacts is bounded by the friction coefficients of the individual materials as measured in similar-contact tests. Based on this, we establish two distinct values of P_{ign} for each stator/rotor pair: one when the friction coefficient equals that of the stator and the other when it equals that of the rotor, both based on similar-contact test data. These two P_{ign} values serve as boundaries for determining safe operating conditions.

Using **Eq. 11**, our previously calculated frictional ignition temperatures for several engineering alloys in similar-contact tests [11], as well as the reported steady-state friction coefficient measured in similar-contact tests [1], we calculate the two P_{ign} values for each material-pair assuming both samples have the same contact-area, a sliding speed of 22 m/s, and an O_2 pressure of 6.9 MPa. Material data used in these calculations is included in **Appendix A**.

Fig. 13 shows P_{ign} values when the friction coefficient is equal to that of the rotor, while **Fig. 14** shows the P_{ign} values when the friction coefficient is equal to that of the stator. The materials are arranged by increasing ignition resistance, with MA956 as the least and MA754 as the most ignition-resistant. Materials with higher ignition resistance exhibit higher maximum allowable contact pressures in identical-contact experiments, further validating the P_{ign} metric. When the friction coefficient is that of the rotor material as shown in **Fig. 13**, using the material with higher ignition resistance as the rotor results in a higher P_{ign} compared to the stator in similar-contact conditions. In contrast, when a more ignition-resistant stator is paired with a less ignition-resistant rotor, the system shows minimal increase in P_{ign}. When the stator material determines the friction coefficient, as shown in **Fig. 14**, the trend reverses, suggesting that the more ignition-resistant material should serve as the stator.

The effect of the friction coefficient on P_{ign} is further emphasized in **Fig. 15**, which plots the absolute difference $|\Delta P_{ign}|$ between the two cases – when the friction coefficient is determined by the rotor or by the stator. A larger $|\Delta P_{ign}|$ reflects greater sensitivity of the maximum allowable contact pressure to the friction coefficient of the sliding system. $|\Delta P_{ign}|$ also emphasizes the uncertainty in the predictions of safe operating conditions for each sliding system between dissimilar materials, highlighting the importance of careful material selection and design when engineering safe, reliable dissimilar sliding contacts. Note that the friction coefficient reflects material transfer from one sample to the other during sliding of dissimilar materials. However, this material transfer process is complex and depends on contact geometry, operating conditions as well as on specific rotor/stator material-pair combinations, suggesting additional dissimilar materials experiments are required to accurately determine the friction coefficient for dissimilar material-pairs.

The above results have significant implications for selecting material pairs for rotor and stator components operating in high-pressure O_2 environments. First, materials with high ignition temperatures should be prioritized to enhance ignition resistance. Second, selecting a stator material with high thermal conductivity can help delay ignition by dissipating heat more efficiently. Improving the convective heat transfer of the rotor, either by optimizing component geometry or using a different cooling fluid, can further help dissipate heat to the gas and delay ignition. Lastly, material pairs should be chosen to facilitate the formation of a thick, lubricating, and protective transfer layer. Therefore, careful consideration must be given to selecting material pairs that allow for substantial tribolayer transfer while mitigating tribolayer breakdown.

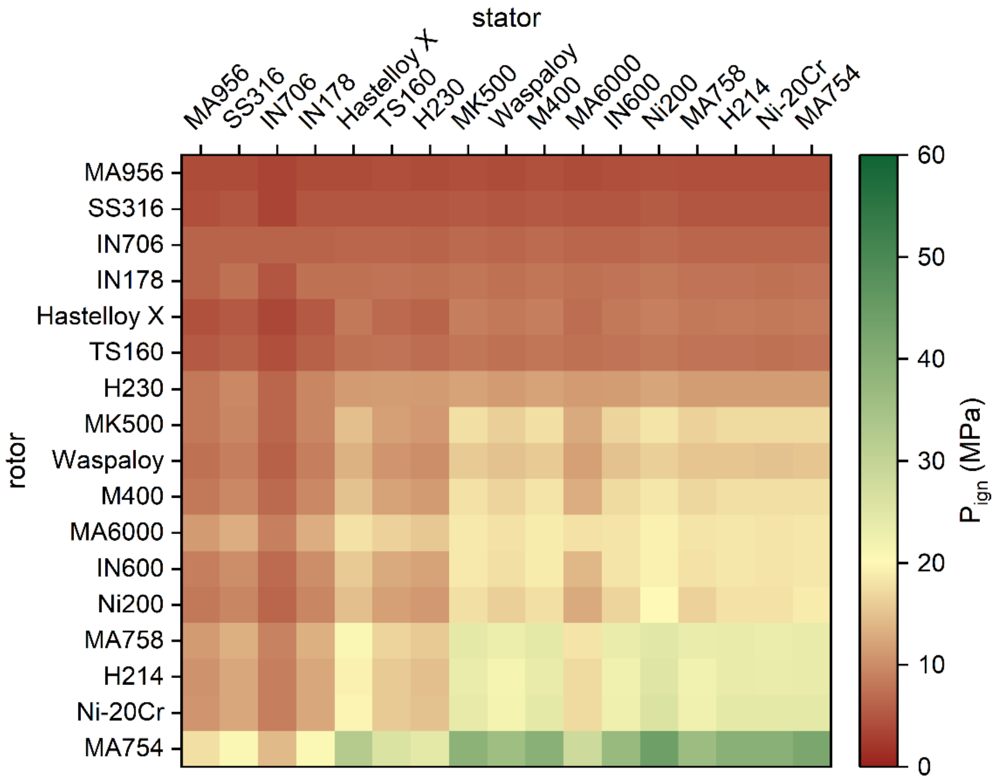

Fig. 13: Maximum allowable contact pressure P_{ign} assuming $v = 22$ m/s and the friction coefficient of the rotor material. Ignition temperature and friction coefficient data retrieved from [1,3,11].

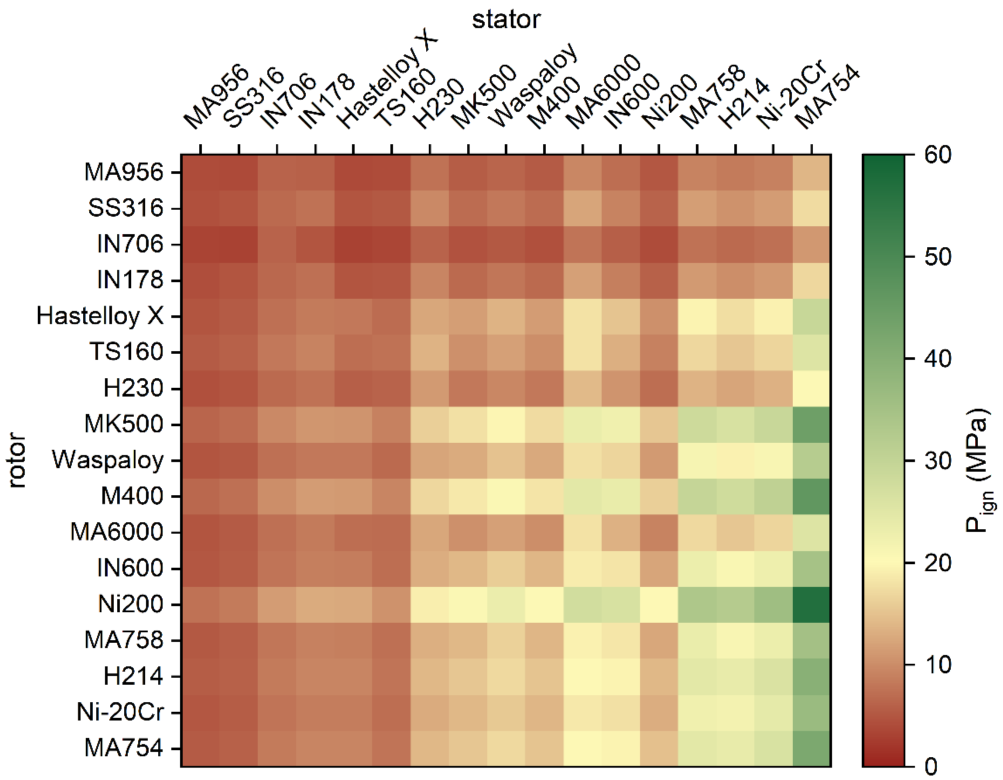

Fig. 14: Maximum allowable contact pressure P_{ign} assuming $v = 22$ m/s and the friction coefficient of the stator material. Ignition temperature and friction coefficient data retrieved from [1,3,11].

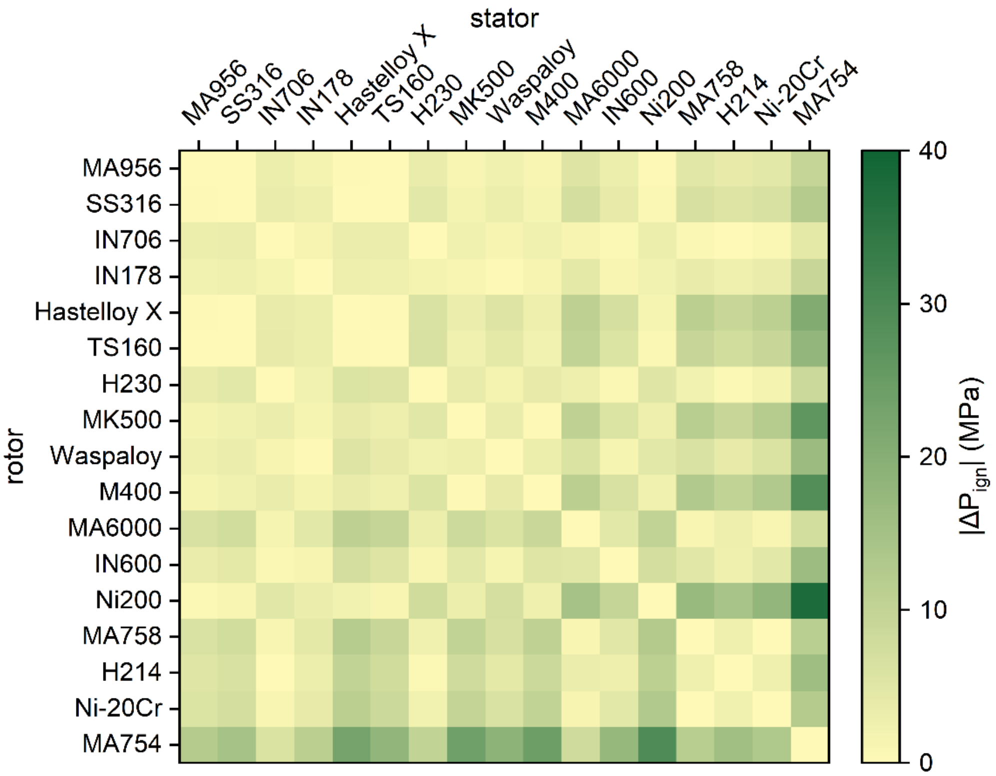

Fig. 15: Difference between the maximum allowable contact pressure P_{ign} when the friction coefficient equals that of the rotor (cf. Fig. 13) and that of the stator (cf. Fig. 14) under v = 22 m/s.

VIII. Conclusions

Frictional heating at dissimilar metal contacts in turbomachinery in high-pressure oxygen-rich environments can result in frictional ignition, a catastrophic failure mode. Here we perform frictional ignition experiments on dissimilar metal contacts between several engineering alloys. The friction coefficient was observed to decay with time, due to the *in situ* growth of a tribolayer at the rubbing interface. The tribolayers on non-ignited samples were characterized to assess the phase distribution and microstructure. Experimental results and finite element simulations were used to compute the surface temperature during sliding and the ignition temperature. A maximum allowable contact pressure metric was developed to determine safe operating conditions for designing frictional ignition-resistant systems. This metric assumes that the contact geometry between the sliding components is the same. Thus, the maximum allowable contact pressure metric must be modified for applications with different contact geometries. Experimental results and observations from the characterization of the tribolayers were integrated with the metric to reveal key trends:

- Tribolayers can form through material transfer from one specimen to another. Consequently, the chemical composition of oxide tribolayers may differ from the parent metals. Material transfer dynamics depend on the stator/rotor material-pair, contact geometry, and sliding conditions.
- The steady-state friction coefficient in dissimilar metal contacts is highly influenced by oxide transfer dynamics and is bounded between the steady-state friction coefficients observed in identical contact tests of each material in the sliding system.
- The ignition temperature of a dissimilar metal pair is determined by the lower ignition temperature of the two constituent alloys from identical contact experiments. Therefore, when designing ignition-resistant sliding systems, it is beneficial to select materials with high ignition temperatures.

- The maximum allowable contact pressure was determined, ensuring the maximum interfacial temperature remains below the ignition temperature, preventing ignition. When the contact pressure exceeds this critical threshold, the interfacial temperature may surpass the ignition temperature, resulting in ignition.
- The maximum allowable contact pressure can be increased, thereby widening the range of operating conditions, by selecting material pairs that have high ignition temperatures, low friction coefficients, and high thermal conductivities. Additionally, enhancing the convective heat transfer coefficient through optimized component geometry or by selecting a cooling fluid with a higher convective heat transfer coefficient can also increase the maximum allowable contact pressure.

Acknowledgments

This research was enabled by financial support from the NSF through grants DMR-2004913 and CMMI–1922206, as well as the Space Systems Command (SSC) under contract FA8802-19-C-0001. A.G.J. gratefully acknowledges support from the NSF Graduate Research Fellowship Program through grant No. 2141064. We thank Dr. Andrew Cortopassi, Dr. Levon Gevorkyan, Dr. Vincent Phong, Armando Perezselsky, and Devon Smith from The Aerospace Corporation for their support with the frictional ignition tests. The authors are also thankful for the ongoing programmatic support of John Di Pol and Dr. James Morehart at The Aerospace Corporation.

References

[1] Stoltzfus JM, Benz FJ, Homa J. The Pv product required for the frictional ignition of alloys. vol. 4, Las Cruces, NM: ASTM International; 1989, p. 212–27.

[2] Benz FJ, Stoltzfus JM. Ignition of Metals and Alloys in Gaseous Oxygen by Frictional Heating. Flammability and Sensitivity of Materials in Oxygen-Enriched Atmospheres: Second Volume, ASTM International; 1986, p. 38–58. https://doi.org/10.1520/STP19308S.

[3] Jimenez AG, Wabel T, Bendana FA, DeSain JD, Xu M, LeBeau JM, et al. Frictional ignition of dispersion-strengthened Ni-Cr alloys. Tribology International 2024:109370. https://doi.org/10.1016/j.triboint.2024.109370.

[4] Fishkis M. Metal transfer in the sliding process. Wear 1988;127:101–10. https://doi.org/10.1016/0043-1648(88)90055-5.

[5] Rigney DA. Transfer, mixing and associated chemical and mechanical processes during the sliding of ductile materials. Wear 2000;245:1–9. https://doi.org/10.1016/S0043-1648(00)00460-9.

[6] Rigney DA, Chen LH, Naylor MGS, Rosenfield AR. Wear processes in sliding systems. Wear 1984;100:195–219. https://doi.org/10.1016/0043-1648(84)90013-9.

[7] Schey JA, Nautiyal PC. Effects of surface roughness on friction and metal transfer in lubricated sliding of aluminium alloys against steel surfaces. Wear 1991;146:37–51. https://doi.org/10.1016/0043-1648(91)90222-G.

[8] Rabinowicz E, Tabor D, Bowden FP. Metallic transfer between sliding metals: an autoradiographic study. Proceedings of the Royal Society of London Series A Mathematical and Physical Sciences 1997;208:455–75. https://doi.org/10.1098/rspa.1951.0174.

[9] Gevorkyan L, McCall S, Smolke J, Driscoll R. A Test Apparatus for the Characterization of Ignitability and Flammability of Metals in High Pressure Oxygen. Propulsion and Energy 2019 Forum, Indianapolis, IN: American Institute of Aeronautics and Astronautics; 2019. https://doi.org/10.2514/6.2019-4351.

[10] Wabel TM, Bendana F, DeSain J, Gevorkyan L. Friction Ignition Testing of Metals in Oxygen up to 24.1 MPa, American Institute of Aeronautics and Astronautics; 2023, p. 1491. https://doi.org/10.2514/6.2023-1491.

[11] Garcia Jimenez A, Cordero ZC. Frictional Ignition of Metals in High Pressure Oxygen: A Critical Reassessment of NASA Test Data, American Institute of Aeronautics and Astronautics; 2023, p. 1489. https://doi.org/10.2514/6.2023-1489.

[12] Anderson JT, Saunders OA, Taylor GI. Convection from an isolated heated horizontal cylinder rotating about its axis. Proceedings of the Royal Society of London Series A Mathematical and Physical Sciences 1997;217:555–62. https://doi.org/10.1098/rspa.1953.0080.

[13] Stewart RB, Jacobsen RT, Wagner W. Thermodynamic Properties of Oxygen from the Triple Point to 300 K with Pressures to 80 MPa. Journal of Physical and Chemical Reference Data 1991;20:917–1021. https://doi.org/10.1063/1.555897.

[14] Lemmon EW, Jacobsen RT. Viscosity and Thermal Conductivity Equations for Nitrogen, Oxygen, Argon, and Air. International Journal of Thermophysics 2004;25:21–69. https://doi.org/10.1023/B:IJOT.0000022327.04529.f3.

[15] McBride BJ, Zehe MJ, Gordon S. NASA Glenn Coefficients for Calculating Thermodynamic Properties of Individual Species. Glenn Research Center: NASA; 2002.

[16] Air Products and Chemicals Inc. Thermodynamic data on oxygen and nitrogen. Wright-Patterson Air Force Base OH: 1961.

[17] COMSOL Multiphysics® v. 6.2. www.comsol.com. COMSOL AB, Stockholm, Sweden. 2024.

[18] Rigney DA, Fu XY, Hammerberg JE, Holian BL, Falk ML. Examples of structural evolution during sliding and shear of ductile materials. Scripta Materialia 2003;49:977–83. https://doi.org/10.1016/S1359-6462(03)00472-X.

[19] Wood GC, Hodgkiess T. Characteristic Scales on Pure Nickel-Chromium Alloys at 800°–1200°C. J Electrochem Soc 1966;113:319. https://doi.org/10.1149/1.2423955.

[20] Wood GC, Wright IG, Hodgkiess T, Whittle DP. A Comparison of the Oxidation of Fe&&bond;Cr, Ni-Cr and Co-Cr alloys in oxygen and water vapour. Materials and Corrosion 1970;21:900–10. https://doi.org/10.1002/maco.19700211105.

[21] Garcia Jimenez A, Wabel T, Bendana F, DeSain J, Gevorkyan L, Cordero ZC. Tribolayer breakdown mechanisms and their role in frictional ignition of metals 2024.

[22] Antler M. Processes of metal transfer and wear. Wear 1964;7:181–203. https://doi.org/10.1016/0043-1648(64)90053-5.

[23] Abdul-Aziz A, Tong MT, Kaufman A. Thermal finite-element analysis of space shuttle main engine turbine blade. Finite Elements in Analysis and Design 1989;5:337–48. https://doi.org/10.1016/0168-874X(89)90012-7.

[24] Brentari EG, Giarratano PJ, Smith RV. Boiling Heat Transfer for Oxygen, Nitrogen, Hydrogen, and Helium. U.S. National Bureau of Standards; 1965.

Appendix A

Table A1: Material data used in calculating maximum allowable contact pressure.

Material	κ (Wm^{-1}K^{-1})	μ	T_{ign} (K)
IN706	12.5	0.034	790
MA956	10.9	0.065	910
SS316	16.3	0.069	1000
H230	8.9	0.035	1130
MA6000	10.8	0.028	1280
TS160	38.0	0.067	1160
Hastelloy X	9.2	0.070	1380
Waspaloy	11.0	0.042	1500
MA758	16.0	0.030	1510
IN600	12.5	0.038	1530
MA754	14.3	0.020	1680
M400	21.8	0.052	1560
Ni200	71.0	0.060	1720
H214	12.0	0.033	1610